The Astrophysical Journal Letters, 990:L60 (13pp), 2025 September 10 https://doi.org/10.3847/2041-8213/adfa97
© 2025. The Author(s). Published by the American Astronomical Society.
OPEN ACCESS

Observational Constraints on the Radial Evolution of O^{6+} Temperature and Differential Flow in the Inner Heliosphere

Yeimy J. Rivera[1], Kristopher G. Klein[2], Joseph H. Wang[3], Lorenzo Matteini[3], Daniel Verscharen[4], Jesse T. Coburn[3], Samuel T. Badman[1], Susan T. Lepri[5], Ryan M. Dewey[5], Jim M. Raines[5], B. L. Alterman[6], Timothy J. Stubbs[7], Kevin C. Delano[6,8], Roberto Livi[9], Stefano A. Livi[5,10], Antoinette B. Galvin[11], Christopher J. Owen[4], and Michael L. Stevens[1]

[1] Center for Astrophysics—Harvard & Smithsonian, 60 Garden Street, Cambridge, MA 02138, USA
[2] Lunar and Planetary Laboratory, University of Arizona, Tucson, AZ 85719, USA
[3] Department of Physics, Imperial College London, London, SW7 2BW, UK
[4] Mullard Space Science Laboratory, University College London, Holmbury St. Mary, Dorking, Surrey, RH5 6NT, UK
[5] Department of Climate and Space Sciences and Engineering, The University of Michigan, Ann Arbor, MI, USA
[6] Heliophysics Science Division, NASA Goddard Space Flight Center, Greenbelt, MD 20771, USA
[7] Solar System Exploration Division, NASA Goddard Space Flight Center, Greenbelt, MD 20771, USA
[8] University of Maryland, Baltimore County, Baltimore, MD 21250, USA
[9] Space Sciences Laboratory, University of California, Berkeley, CA 94720, USA
[10] Southwest Research Institute, San Antonio, TX 78228, USA
[11] University of New Hampshire, Durham, NH, USA
Received 2025 July 11; revised 2025 July 30; accepted 2025 August 10; published 2025 September 8

Abstract

Over decades of solar wind observations, heavy ions have been observed to have a higher temperature and flow faster than protons in the solar corona and heliosphere. Remote observations have largely been limited to the low corona ($<4\ R_\odot$), while in situ observations for heavy ions ($Z > 2$) have only been sampled at 1 au and beyond. As a result, theories that address heavy ion heating and acceleration remain largely unconstrained. With the launch of Solar Orbiter, heavy ion kinetics can be probed closer to the Sun, as close as the orbit of Mercury (65 $R_\odot$), to examine their radial behavior. Through a statistical analysis of O^{6+}, this work provides a comprehensive analysis of the velocity and temperature of O^{6+} from 0.3 to 1 au. The study finds that the O^{6+} relative drift, normalized to the local Alfvén speed, and its temperature compared to protons both decrease with distance from the Sun and show some speed dependence. The O^{6+} temperature is well fit by a single temperature adiabatic profile across all wind speeds, suggesting that there is no significant heating at these heliocentric distances, which is in contrast to what is observed for protons and He^{2+}. Alfvénic fluctuations, some with full 180° field rotation, create momentary negative differential streaming where the speed of O^{6+} trails the protons. The amount of negative differential streaming gradually increases at larger distances. These results provide critical constraints on the proposed mechanisms seeking to describe ion heating and acceleration in the solar wind.

Unified Astronomy Thesaurus concepts: Solar wind (1534); Alfvén waves (23); Space plasmas (1544); Chemical abundances (224)

1. Introduction

The Sun creates a continuous stream of outflowing plasma called the solar wind. The solar wind quickly expands as it escapes the magnetically dominated corona to fill the heliosphere. As the plasma expands, Coulomb collisions become less frequent as it transitions into a hot, collisionless plasma. Low in the corona, Coulomb collisions regulate particle distributions by continuously redistributing energy among the ions and electrons, which maintain isotropic, Maxwellian velocity distributions. When collisions become less frequent, as the solar wind becomes more and more tenuous, nonthermal particle distributions are observed. These nonthermal distributions can be identified by high-energy ion and electron tails and beams, temperature anisotropies with respect to the background magnetic field, and differential heavy ion flows (E. Marsch et al. 1982b; E. Marsch 2006; B. L. Alterman et al. 2018; D. Verscharen et al. 2019; J. L. Verniero et al. 2020). The competition of collisions, waves/instabilities, and ongoing turbulence processes is responsible for the energy exchange and partitioning among ions and electrons, which can drive the heating and acceleration observed in the corona and throughout the inner heliosphere (C. Y. Tu & E. Marsch 1995; L. Adhikari et al. 2021; C. A. González et al. 2021; N. Sioulas et al. 2022; R. Bandyopadhyay et al. 2023; J. S. Halekas et al. 2023; S. Bourouaine et al. 2024; Y. J. Rivera et al. 2024, 2025; N. Shankarappa et al. 2024; A. Silwal et al. 2025).

In collisional thermodynamic equilibrium, the ions and electrons are described by a single temperature and flow speed. However, deviations from equilibrium are often observed, even in the corona, as nonthermal features develop as close as 1 $R_\odot$ from the solar surface in coronal holes. The UltraViolet Coronagraph Spectrometer (UVCS; J. L. Kohl et al. 1995) on the Solar and Heliospheric Observatory (SOHO) satellite detected deviation from thermal equilibrium using spectral observations of the O VI 1032 and 1037 Å doublet, or O^{5+}. The oxygen was measured to flow at twice the proton speed while having a super-mass-proportional temperature, $T_{O5+}/T_p > 16$, and notable O^{5+} temperature anisotropies, $T_\perp/T_\parallel > 10$, by

Original content from this work may be used under the terms of the Creative Commons Attribution 4.0 licence. Any further distribution of this work must maintain attribution to the author(s) and the title of the work, journal citation and DOI.

2 $R_\odot$ (J. C. Raymond et al. 1997; S. R. Cranmer 2009). Mg X 1219.71 Å, or Mg^{9+}, was also observed to be superheated, like oxygen. These observations suggest that nonthermal processes in coronal hole wind are more effective at heating O^{5+} (and Mg^{9+}) compared to protons, and the heating is preferentially perpendicular to the local magnetic field direction. Several studies suggest that Alfvén cyclotron waves can resonantly transfer energy to the ions, leading to preferentially perpendicular heating as they dissipate that reconciles the heavy ion observations (Y. Q. Hu & S. R. Habbal 1999; J. V. Hollweg & P. A. Isenberg 2002; J. C. Kasper et al. 2008), with recent near-Sun observations identifying their presence in the solar wind reinforcing this theory (W. Liu et al. 2023; T. A. Bowen et al. 2024a, 2024b). However, the process by which the waves are generated and how dissipation occurs remains difficult to pin down (E. Marsch & C. Y. Tu 2001; J. V. Hollweg & P. A. Isenberg 2002; S. R. Cranmer & A. A. van Ballegooijen 2003; P. Hellinger et al. 2005; P. A. Isenberg & B. J. Vasquez 2007, 2009; S. R. Cranmer & A. R. Winebarger 2019; G. G. Howes 2024).

Other mechanisms have been proposed. Stochastic heating via dissipation of low-frequency turbulence could also explain the observed heavy ion temperatures (B. D. G. Chandran 2010; B. D. G. Chandran et al. 2013). The so-called "helicity barrier" offers an avenue for ion cyclotron heating, in line with theory and observations, that may unify wave and turbulence theories addressing ion heating (R. Meyrand et al. 2021; J. Squire et al. 2022; U. Panchal et al. 2025; M. F. Zhang et al. 2025). Most recently, several studies have explored the role of kinetic Alfvén waves in ion heating and acceleration in the 1–10 $R_\odot$ regime that would also be compatible with coronal observations (S. Ayaz et al. 2024, 2025a, 2025b).

The nonthermal characteristics extend and continue to evolve in the heliosphere. Several studies have found that the differential streaming of helium can be as large as the Alfvén speed (V_A), as observed with Helios 1 and 2 between 0.3 and 1 au (E. Marsch et al. 1982a; T. Durovcová et al. 2019), while continuing to decrease beyond 1 au as observed with Ulysses (M. Neugebauer et al. 1996; D. B. Reisenfeld et al. 2001). Additionally, the scalar temperature of helium is observed to be higher than protons to varying degrees, often exceeding mass proportionality, i.e., becoming super-mass-proportional (J. C. Kasper et al. 2008; B. A. Maruca et al. 2013).

Most recently, observations from Parker Solar Probe (Parker; N. J. Fox et al. 2016) have provided new insight into the kinetics of helium below 0.3 au (P. Mostafavi et al. 2022). Studies find that larger differential speeds between He^{2+} and protons ($V_{He2+,p} = V_{He2+} - V_p$) are correlated to higher temperature ratios, T_{He2+}/T_p, at these distances (J. Peng et al. 2024). The observations in the study suggested a preferential heating zone for He^{2+} that is below 0.16 au (or $\sim$34 $R_\odot$). This is in line with other studies that predict that the majority of preferential heating occurs below the Alfvén surface (J. C. Kasper et al. 2017; J. C. Kasper & K. G. Klein 2019), while that distance varies for heavier ions (J. Holmes et al. 2024). Studies have also found that differential flow of He^{2+} reaches a maximum of 100–200 km s^{-1}, despite an increasing Alfvén speed closer to the Sun (J. H. Wang et al. 2025).

Prior to the launch of Solar Orbiter (D. Müller et al. 2020) in 2020, heavier ions ($Z > 2$, where Z is the atomic number or number of protons) have only been examined between 1 and 5 au with the Solar Wind Ion Composition Spectrometer (SWICS) on board both the Advanced Composition Explorer (ACE) and Ulysses, the Charge Time-of-Flight solar wind ion sensor on SOHO (S. Hefti et al. 1998; N. P. Janitzek et al. 2016), and STEREO/PLASTIC (P. Bochsler et al. 2010a, 2010b). From ACE/SWICS observations, L. Berger et al. (2011) examined the differential flow ($V_{i,p} = V_i - V_p$) of 44 heavy ions at L1 across mass (m = 4–56 amu) and mass-per-charge (m/q = 2–8 amu e^{-1}) for a 2 week period in a predominately fast wind stream. The study finds that, on average, the minor ions stream at 0.55 V_A, with no clear m/q or m dependence. The majority of differential streaming was positive with a few instances of negative differential streaming that the authors attribute to kinks in the magnetic field. In the same systematic manner, P. J. Tracy et al. (2015, 2016) examine the temperature and thermal speed of 50 minor ions, organized by collisional age, observed at 1 au from 13 yr of data. The collisional age is an in situ, single-point estimate of the cumulative effect of Coulomb collisions—normalizing the collision frequency to the transit time of a plasma parcel—that would act to thermalize the solar wind and erase nonthermal signatures (J. C. Kasper et al. 2008; B. L. Alterman et al. 2018; M. M. Martinović et al. 2021), including any super-mass-proportional temperature observed in the corona. Near 1 au, the temperature of O^{6+} ($m/q = 16/6 = 2.67$) and several other ions compared to that of protons (T_i/T_p) shows a convergence toward unity at the highest collisional ages. However, the temperature ratio did not strictly decrease, suggesting more complex behavior across solar wind speed and its radial evolution.

In addition to collisions, wave–particle interactions may explain the simultaneous decrease in differential flow and increase in temperature of the He^{2+} population. For example, 2D hybrid simulations of collisionless plasma show that wave–particle scattering via alpha–proton parallel magnetosonic and Alfvén instabilities reduces the relative flow between helium and protons, heats the helium more strongly than the protons, and increases the $T_\perp/T_\parallel$ of the helium, in line with the radial profiles seen in He^{2+} observations (S. P. Gary et al. 2000). In addition, the theoretical framework of stochastic heating from B. D. G. Chandran et al. (2013) also finds an inverse relationship between differential flow and the perpendicular temperature ratio of He^{2+} to protons, matching well with observations from the Wind spacecraft (J. C. Kasper et al. 2013). However, it is unknown if heavier ions behave in the same manner and can be described the same way by these processes.

Further evaluation of several theories and models requires extended knowledge of minor ion temperatures and speeds at several stages of solar wind outflow. As such, this work examines the radial evolution of O^{6+} drift speed and temperature between 0.3 and 1 au to analyze its behavior in the solar wind.

2. Observations

The study utilizes observations taken by the Heavy Ion Sensor (HIS; S. Livi et al. 2023), part of the Solar Wind Analyzer (SWA; C. J. Owen et al. 2020) suite on Solar Orbiter, across a 1 yr and 4 month period during the ascending phase of solar cycle 25. To examine the radial evolution of differential streaming and temperature together, we use the O^{6+} speed and temperature from V02 of the HIS Level 3 data set (released December 2024[12]). In this version, the HIS data set includes

[12] https://www.cosmos.esa.int/documents/3689933/11863906/SWA-HIS_usage_notes_L3_V02.pdf

10 minute cadence observations of oxygen and carbon ion ratios, iron charge-state distribution, and the Fe/O abundance ratio. This data set also includes O^{6+} bulk and thermal speeds, with more heavy ion kinematics planned for future releases. This study therefore focuses on these properties of O^{6+}.

The study uses measurements of the magnetic field and proton speed, temperature, and densities taken by the magnetometer on board (MAG; T. S. Horbury et al. 2020) and Proton Alpha Sensor (PAS) of SWA, respectively. To compute the different quantities, the measurements from PAS and MAG have been averaged down to match the 10 minute HIS resolution.

The period examined spans from 2022 January 1 to 2023 April 30. The trajectory of Solar Orbiter during this period is shown in Appendix Figure A1. The period includes three perihelia, with closest approaches on 2022 March 26, 2022 October 12, and 2023 April 10. To ensure that the majority of the analysis included only nontransient solar wind, we removed coronal mass ejections (CMEs) as identified in the Helio4Cast catalog (C. Möstl et al. 2017, 2020).[13] After the removal of CME periods, the number of 10 minute intervals considered in the study is $N = 40{,}613$.

We compute differential streaming normalized to the Alfvén speed ($V_{O6+,p}/V_A$) using the magnitude of the proton speed in the spacecraft frame and of the O^{6+} speed, where we assume that the bulk speed is dominated by the radial component. We use the spacecraft frame, where the $-X$ component is aligned with the radial component (R) in the RTN system, such that the difference between O^{6+} and protons eliminates the spacecraft speed. The Alfvén speed is computed as $V_A = \frac{B}{\sqrt{\mu_0 m_p n_p}}$, where B is the magnetic field strength, μ_0 is the permeability of free space, and m_p and n_p are the mass and number density of protons.

We now develop a prediction for the dependence of the relative drift on the angle Θ between the radial direction and the local magnetic field. We assume that the relative drift of heavy ions is aligned with the magnetic field. Moreover, we assume that any dependence of the relative drift on Θ is due to radial variations of the magnetic field, e.g., in the form of localized kinks or large-scale variations. Therefore, we set

$$\boldsymbol{V}_{O6+} = \boldsymbol{V}_p \pm \Delta U\, \hat{\boldsymbol{b}}, \tag{1}$$

where $\boldsymbol{V}_{O6+}$ is the bulk velocity of O^{6+}, $\boldsymbol{V}_p$ is the bulk velocity of the protons, ΔU is the magnitude of the relative drift between O^{6+} and protons, and $\hat{\boldsymbol{b}} = \boldsymbol{B}/B$ is the unit vector of the magnetic field. Assuming that heavy ions are preferentially accelerated in the corona, we choose the upper sign in Equation (1) for measurements in a sector with antisunward magnetic field connectivity and the lower sign for measurements in a sector with sunward magnetic field connectivity. As we measure the radial components of the bulk velocities $V_{O6+,r}$ and $V_{p,r}$, we take the scalar product of Equation (1) with the unit vector $\hat{\boldsymbol{r}}$ in the radial direction and find

$$\frac{V_{O6+,p}}{V_A} = \frac{V_{O6+,r} - V_{p,r}}{V_A} = \pm\frac{\Delta U}{V_A}\cos\Theta, \tag{2}$$

where $\cos\Theta = \hat{\boldsymbol{r}} \cdot \hat{\boldsymbol{b}}$. Our measurement of $V_{O6+,p}/V_A$ thus depends on the relative drift $\Delta U/V_A$ in the field-aligned reference frame and the angle Θ. For $0 < \Theta < \pi/2$, we find $V_{O6+,p}/V_A > 0$ in sectors with antisunward magnetic field connectivity and $V_{O6+,p}/V_A < 0$ in sectors with sunward magnetic field connectivity. For $\pi/2 < \Theta < \pi$, we find $V_{O6+,p}/V_A > 0$ in sectors with sunward magnetic field connectivity and $V_{O6+,p}/V_A < 0$ in sectors with antisunward magnetic field connectivity. Therefore, we predict that all measurements with $V_{O6+,p}/V_A < 0$ represent times in which the magnetic field is locally directed opposite to the direction associated with the global sector (e.g., through a local kink in the field that changes the sign of B_r).

We compute the O^{6+} scalar temperature from the thermal velocity as

$$v_{O6+,th} = \sqrt{\frac{2k_B T_{O6+}}{m_{O6+}}},$$
$$T_{O6+} = \frac{m v_{O6+,th}^2}{2k_B}, \tag{3}$$

where k_B is the Boltzmann constant and m_{O6+} and $v_{O6+,th}$ are the O^{6+} mass and thermal speed.

3. Results

Figure 1 presents 2D histograms, referred to as "moth plots," that show the distribution of counts (left) and the corresponding mean temperature ratio (T_{O6+}/T_p; right) as a function of differential streaming ($V_{O6+,p}/V_A$) and angle between the radial direction and the magnetic field (Θ) in radians. We overplot Equation (2) for different $\Delta U/V_A$ for reference with amplitudes of 1.3, 0.87, and 0.43. The plot on the left incorporates all points measured, and the right plot only includes bins that contain at least five counts to compute the mean of the temperature ratio.

We find that in contrast to L. Berger et al.'s (2011) Figure 3, both plots of Figure 1 show that the parameter space is filled in simply by virtue of including a longer time frame of observations, with more solar wind conditions. We also note that the figure incorporates differential streaming of all solar wind streams measured between 0.3 and 1 au, with observations including different stages of evolution that collapse time and space. Despite this, we see organized behavior in the differential streaming when viewed together. The largest differential flows are observed during field-aligned periods that decrease as the magnetic field is perpendicular to the flow, consistent with our prediction in Equation (2). As in L. Berger et al. (2011), we also find periods of negative differential streaming in O^{6+}, albeit not symmetrically distributed between positive and negative differential flows. This is discussed further in Section 4.4.

There is a significant population of solar wind with differential streaming speeds that are larger than the local Alfvén speed, requiring $V_{O6+,p}$ 30% larger than V_A. Through a comparison with the O^{6+}-to-proton temperature ratio, in the right panel of Figure 1, we find that larger differential speeds correspond to the largest average temperature ratios. The temperature ratio decreases with lower differential speed, with the lowest ratios within periods of negative differential streaming. To disentangle how the O^{6+} temperature and relative flow change with distance from the Sun and solar wind speed within the moth plot parameter space, we also include

[13] https://helioforecast.space/icmecat

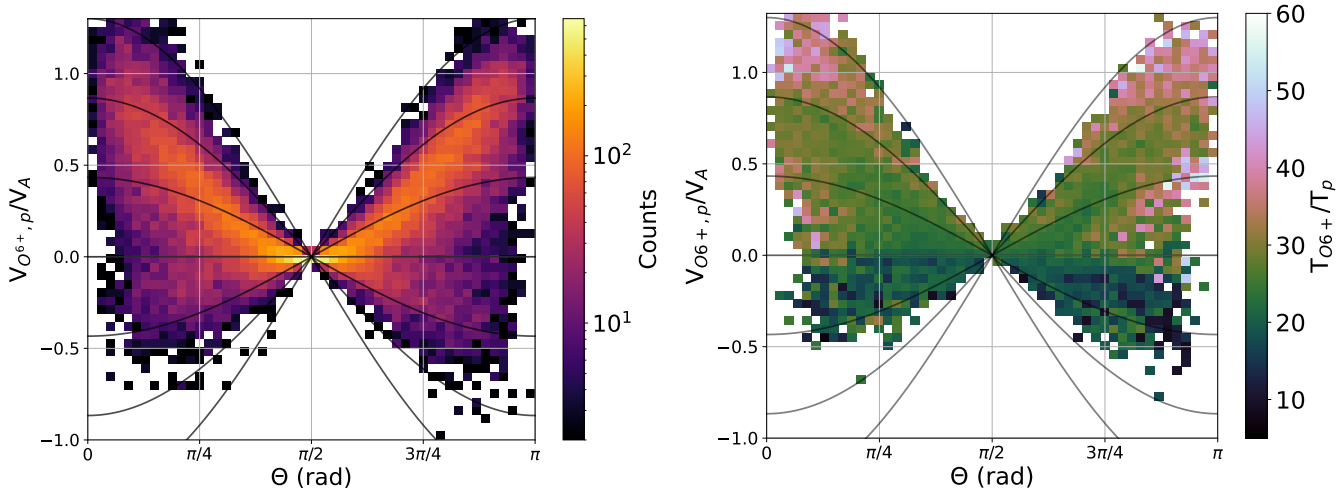

Figure 1. The 2D histograms of differential streaming of O^{6+} normalized to the local Alfvén speed vs. angle between the radial direction and the local magnetic field, which we refer to as a "moth plot." The left panel shows the distribution of all measurements taken, while the right panel shows the average temperature ratios (T_{O6+}/T_p) within the parameter space for bins that contain at least five points. We overplot (solid lines) Equation (2) for different $\Delta U/V_A$ for reference with amplitudes of ±1.3, 0.87, 0.43, and 0.

Figures B1 and B2 in Appendix B, which subcategorizes both panels from Figure 1.

We further examine the radial evolution of O^{6+} differential flow and temperature in Figure 2. The figure includes four panels showing the absolute values of differential streaming normalized to the local Alfvén speed × cos Θ (top left) and just the speed difference (top right) as well as the temperature ratio (T_{O6+}/T_p) and O^{6+} temperature (bottom row), all with increasing distance from the Sun. In the top left plot, we divide the relative flow by cos Θ and only include $\Theta < 1$ and >2.2 (rad) to avoid dividing near 0 and the positive differential streaming periods. The purpose is to remove the variability of differential streaming due to fluctuations that act to reduce the projected relative flow and to only consider the background speed difference (later discussed in Section 4.4). For each case, the solar wind is binned by proton speed (five speed quantiles) and distance from the Sun (seven equally spaced bins): 349–389, 390–440, 441–500, 501–574, and 575–900 km s^{-1} and 0.3–0.43, 0.44–0.57, 0.58–0.7, 0.71–0.83, 0.84–0.97, and 0.98–1.1 au. The background of each plot shows the column-normalized total counts within the parameter space. The vertical bar for each is computed as the standard deviation of the mean.

Generally, all the parameters plotted in Figure 2 decrease with distance from the Sun. As has been observed with He^{2+} in the past at 0.3 au and beyond (E. Marsch et al. 1982a; P. Mostafavi et al. 2022), O^{6+} is also observed to decrease in its differential streaming and to have comparable speed differences ($V_{O6+,p}$, as in the top right panel). In this analysis, some speed dependence arises, although the overall decrease in differential streaming behavior is similar across all solar wind measured. At 1 au, our results show that the range of mean differential flow (top left) across all wind speeds spans between 0.4 and 0.8 V_A. At 1 au, L. Berger et al. (2011) find an average differential flow of heavy ions to be 0.55 V_A, with O^{6+} being slightly larger than the average at 0.6 V_A, as indicated by the green star in the top left panel of the figure. Overall, the differential steaming from the present study (for the fastest speed bin; yellow curve) and ACE/SWICS from L. Berger et al. (2011; mainly for a fast wind stream) at 1 au coincide well.

For the temperature (bottom row of Figure 2), we find that the temperature ratio decreases while remaining super-mass-proportional ($T_{O6+}/T_p > 16$) out to 1 au. Additionally, we find that the O^{6+} population on average cools adiabatically between 0.3 and 1 au, as indicated by the $T \propto r^{-4/3}$ fitted profiles (represented as dashed lines for each speed bin), assuming an adiabatically expanding ideal gas (S. J. Schwartz & E. Marsch 1983). The profiles use an initial temperature from 0.3 au as the first value of each curve and are extrapolated to 1 au. Together, these observations suggest that strong preferential heating of O^{6+} has finished well below 0.3 au and directly shows that no significant local heating occurs beyond this distance. Furthermore, we compare observations to previous studies: P. J. Tracy et al. (2016), as indicated by the pink star, and a prediction from J. Holmes et al. (2024), shown as the white star in the bottom left panel, which is discussed in Section 4.2.

4. Discussion

4.1. O^{6+} Temperature and Relative Flow

Generally, we find that the average differential flow between O^{6+} and protons is reduced with radial distance while its radial scalar temperature profile indicates no strong heating, as shown in Figure 2. This behavior deviates from what is observed in He^{2+} radial studies, where T_{He2+} shows nonadiabatic cooling similar to protons while reducing its differential flow (T. Durovcová et al. 2019; J. Peng et al. 2024). In our analysis, we note that an adiabatic temperature profile, ($1/r^{4/3}$), may not be strictly true for a turbulent, collisionless plasma with strong temperature anisotropies such as the solar wind, which can drive instabilities and depart from an ideal gas (L. Matteini et al. 2007, 2012). Statistically, temperature anisotropies ($T_\perp/T_\parallel$) are observed for protons and alpha particles and increase for both with solar wind speed (E. Marsch et al. 1982b). Several studies have examined the role of instabilities as the driver of proton and helium temperature and differential flow behavior (S. P. Gary et al. 2000; B. A. Maruca et al. 2012; B. D. G. Chandran et al. 2013; D. Verscharen et al. 2013; M. D. McManus et al. 2024; M. M. Martinović et al. 2025). In linear Vlasov theory, proton

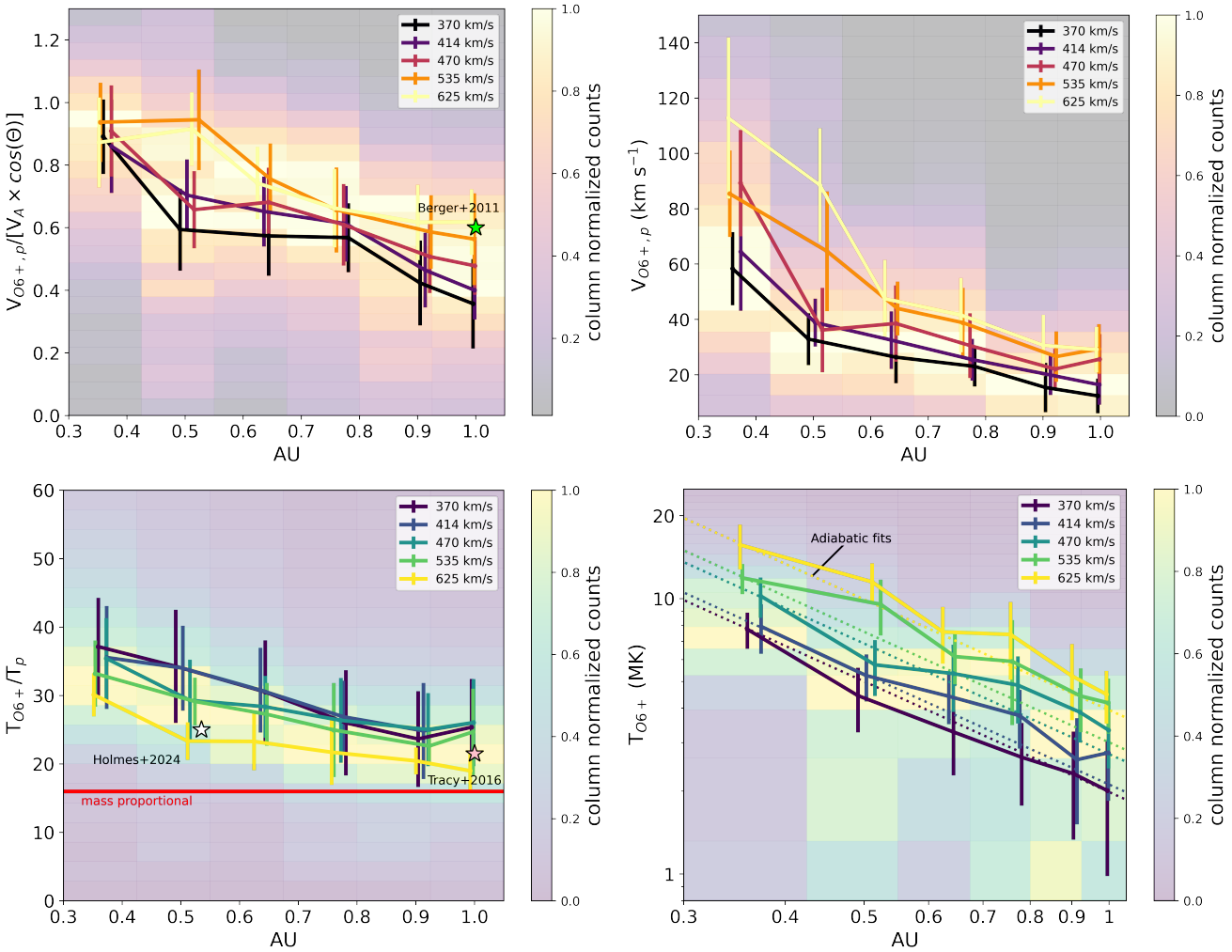

Figure 2. The 2D histograms and radial profiles of O^{6+} (top left) differential flow normalized to the local Alfvén speed $\times \cos\Theta$, (top right) differential streaming, (bottom left) scalar temperature ratio with protons, and (bottom right) temperature, all plotted against heliocentric distance from the Sun in au. The bottom right plot has a log-log scale, while the others are in linear scale. The background histograms are a distributions of counts in this parameter space that are column-normalized. The radial profiles have been binned by proton speed, where the mean is reported in the legend; see Section 3 for bin ranges. In the top and bottom left plots, we include observations of O^{6+} from L. Berger et al. (2011) and P. J. Tracy et al. (2016) as well as a prediction from J. Holmes et al. (2024).

and alpha temperature anisotropies can both be constrained by various kinetic instabilities: cyclotron, mirror, and parallel and oblique firehose. These instabilities impose limits to their temperature anisotropy ratios that inhibit unbounded growth or decay. Observations of minor ions indicate strong temperature anisotropies in the corona that may extend to the solar wind, driving instabilities that modulate its observed scalar temperature. Therefore, in addition to the scalar temperature examined in the present study, it is crucial to inspect O^{6+} temperature anisotropy in more detail to account for anisotropic heating that is not directly observable in the present study.

4.2. O^{6+} Zone of Preferential Heating

Comparison between the in situ speed and temperature profiles against those observed at the Sun provides some bounds to the zone of preferential oxygen heating. The radial temperature profiles and adiabatic temperature fits of O^{6+} suggest that the majority of heating it experiences occurs below 0.3 au. Figure 2 (bottom left panel), which shows the temperature ratio (T_{O6+}/T_p), includes the temperature ratio predicted by J. Holmes et al. (2024) for the outer radial boundary of the zone of preferential heating for O^{6+}. The outer radial boundary represents the location where preferential heating of minor ions is active. The value predicted by J. Holmes et al. (2024), represented by a white star, is on the order of 25 and falls within the range of average values computed for the fastest wind (yellow curve). However, the value from J. Holmes et al. (2024) would not be compatible with excess local heating up to the predicted outer radial boundary of 115 $R_\odot$ (0.54 au) given that the temperature shown in the bottom right panel is well described by adiabatic cooling starting at 65 $R_\odot$ (0.3 au).

Additionally, we compare our results to temperature observations at 1 au from P. J. Tracy et al. (2016). The study finds an average behavior of $\frac{T_i}{T_p} = \frac{4}{3}\frac{m_i}{m_p}$ for ions, i, as determined through a simple linear fit to heavy ion temperatures from 13 yr of observations. Therefore, the temperature ratio for O^{6+} should be on the order of 21.3 at the outer edge of our observation domain, as indicated by the pink star at 1 au in the figure. Our results show that the average temperature ratio and its variability across wind speeds falls within the predicted value of P. J. Tracy et al. (2016).

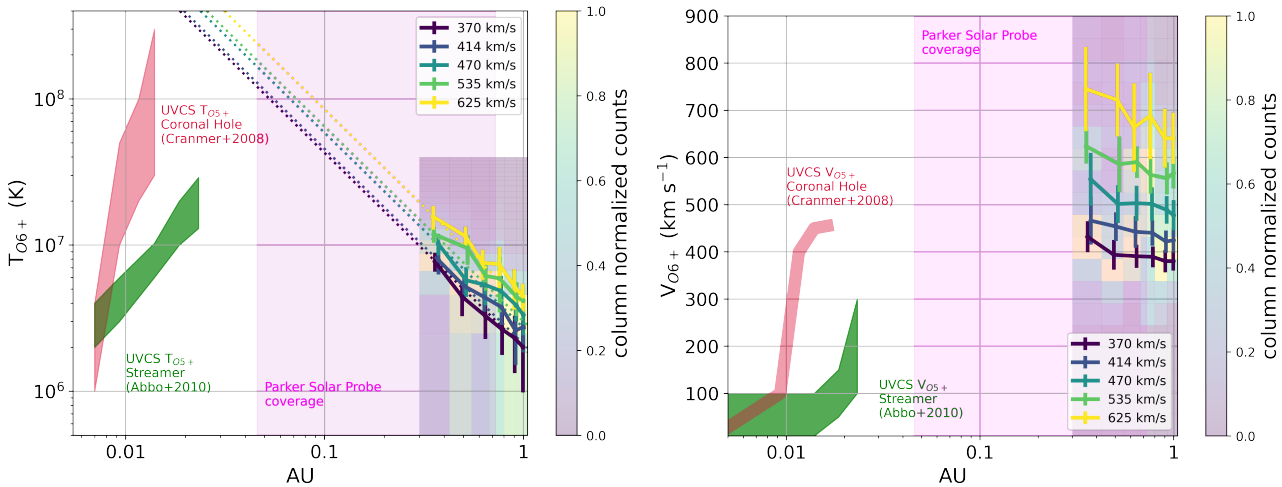

Figure 3. High charge states of oxygen in the inner heliosphere: O^{6+} temperature and speed vs. heliocentric distance to the Sun between 0 and 1 au. The plots include observations from UVCS of O^{5+} in a polar coronal hole from S. R. Cranmer et al. (2008) and a streamer from L. Abbo et al. (2010, 2016), whose ranges are indicated by the red and green regions, respectively, extending between approximately the solar surface and 0.0186 au (1−4 $R_\odot$). We also include the coverage of Parker between ∼9.86 and 155 $R_\odot$.

4.3. Comparison to Remote Observations of Oxygen

Figure 3 shows a comparison of the present analysis of O^{6+} (taken during the ascending phase of the solar cycle) to O^{5+} temperature and speed at the Sun observed in a polar coronal hole (red) with UVCS/SOHO between 1996 and 1997 (S. R. Cranmer et al. 2008) and an equatorial streamer (green) in solar minimum (L. Abbo et al. 2010, 2016). We note that heavy ion properties in the slow solar wind do exhibit some solar cycle dependence (D. T. Carpenter et al. 2024; B. L. Alterman et al. 2025a, 2025b). Therefore, some solar cycle variation may be present when comparing the remote observations of the streamer (taken in solar minimum), which we connected to the slow solar wind properties (taken in the ascending phase). The figure also includes the present Parker coverage that spans 9.86–155 $R_\odot$ for reference. Within the remote observations, the temperature increases between 1×10^6 and 2×10^8 K while increasing in speed from 20 to 500 km s^{-1} across a heliocentric distance of 1−3.5 $R_\odot$ in the coronal hole. At the outer edge of the field of view, the temperature ratio of the coronal hole would correspond to $T_{O5+}/T_p = 23.5$ (S. R. Cranmer 2020). In the streamer, the temperature increases from 2×10^6 to 3×10^7, and its outflow speed increases more gradually, reaching just below 300 km s^{-1} by 5 $R_\odot$. At the outer edge of the streamer measurements, the average $T_{O5+}/T_p = 21$.

The extrapolations of the O^{6+} adiabatic temperature fits back to the Sun show that the temperature, if simply adiabatically expanding and cooling, would exceed the measured values observed in the low corona. The fitted profiles (if valid) would suggest that the temperature of O^{6+} would continue to rise, peak, and turn over just after leaving the field of view of UVCS at 3.5−5 $R_\odot$. Under the assumption of a nearly constant proton temperature in the corona, this would also be supported by the measured temperature ratio of $T_{O5+}/T_p = 23.5$ and 21 between 3.5 and 5 $R_\odot$. This ratio is lower and would be required to increase to match observations at 0.3 au which falls between 30 and 40 as shown in Figure 2, bottom left panel. However, this is difficult to disentangle because there are no observations of heavy ion properties above a few solar radii from the solar surface or below 65 $R_\odot$.

In the speed profile shown in the right panel of Figure 3, the edge of the UVCS field of view sees a plane-of-the-sky outflow velocity of 500 km s^{-1} in a coronal hole and up to 300 km s^{-1} in a streamer for O^{5+}. The in situ O^{6+} speed is measured to be between 400 and 800 km s^{-1} near 0.3 au, where the yellow curve in the figure at 700–800 km s^{-1} would best coincide with polar coronal hole observations, while the dark purple curve would correspond to the streamer coronal observations. Together, these observations suggest that O^{5+} and O^{6+} experience acceleration beyond the UVCS field of view in order to match the speed observed in situ.

4.4. Negative Differential Streaming Behavior during Alfvénic Fluctuations

As observed in Figure 1 and Appendix Figure B2, there are case studies of significant negative differential flow between O^{6+} and protons related to local reversals in the magnetic field, as predicted from Section 2. The magnetic reversals are Alfvénic fluctuations that show a correlated magnetic and velocity fluctuation that indicates high cross-helicity. Figures 4 and 5 show examples during these periods that occurred on 2022 December 22 near 0.921 au and 2023 April 22 between 0.384 and 0.39 au. The top row of panels shows the moth plot from Figure 1 in the background, cos(Θ) curves, and the measurements of differential streaming versus Θ across the shaded magenta period of the time series below. The magenta period encompasses the fluctuation period of interest. The colors in each top panel correspond to the color bar showing the magnetic field polarity (red is positive and blue is negative; top left), O^{6+} speed in km s^{-1} (top middle), and magnetic fluctuation normalized to the 2 hr mean field magnitude ($\delta b/B$; top right). We compute δb as $|\delta \boldsymbol{b}| = \boldsymbol{B} - \langle \boldsymbol{B} \rangle_t$, where $\langle \boldsymbol{B} \rangle_t$ is time-averaged over a 2 hr interval, t. The time series (bottom left) shows the magnetic field magnitude (black) and B_R (red/blue) along with $V_{O6+,p}/V_A$ (gray). These measurements were taking in a sector of antisunward magnetic field connectivity. The middle panel contains the proton and O_{6+} speed and $V_p + V_A$ (red), and the bottom panel shows the individual temperature and ratio. Lastly, in Figure 4, the bottom right panel shows a modified image of a lever-arm picture from

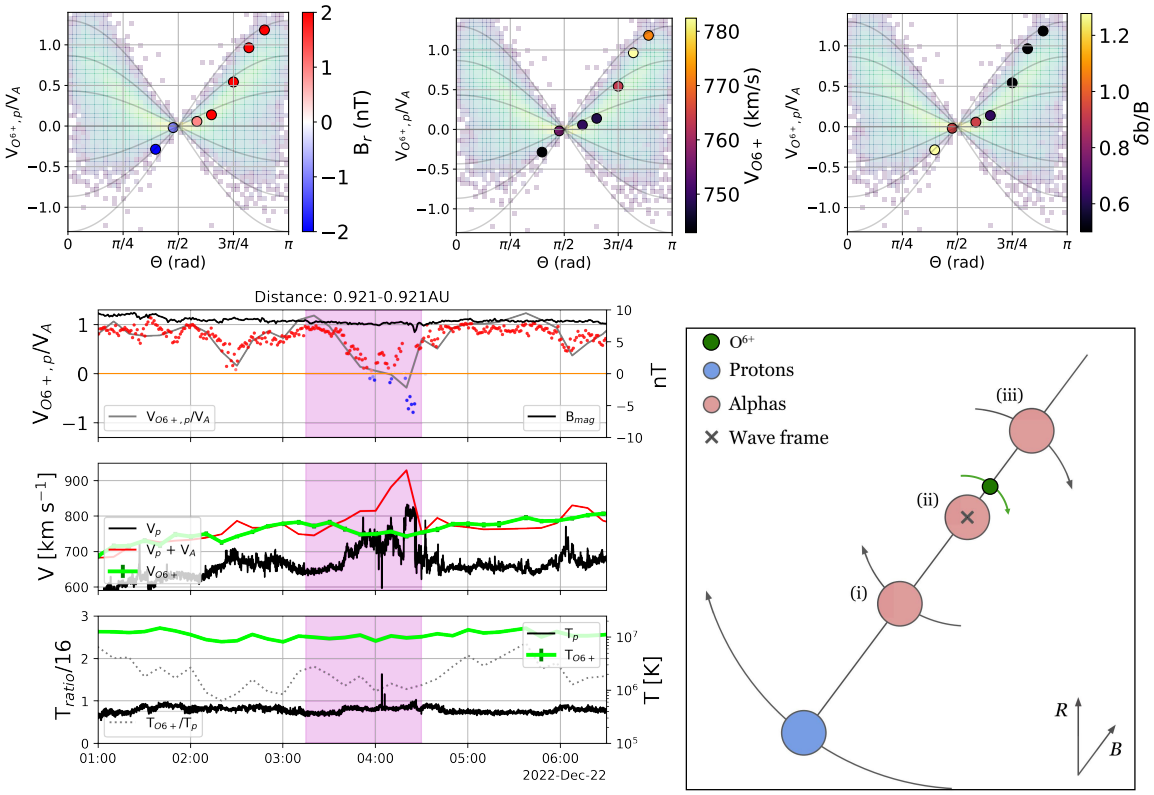

Figure 4. Negative differential streaming periods due to an Alfvénic fluctuation. The top row shows three panels of 2D histograms with the radial component of the magnetic field, V_{O6+}, and $\delta B/B$ values across an individual Alfvénic fluctuation period highlighted in the shaded region shown in the time series below. In the time series plots, the top panel shows differential streaming in gray in association with the left vertical axis and the radial magnetic field, B_R (where red is for positive and blue is for negative polarity), and magnitude, B, in black. The middle panel shows the proton (black) and O^{6+} (green) speed magnitude along with the proton + Alfvén speed (red). The bottom panel shows the proton and O^{6+} individual temperatures (right vertical axis; black and green, respectively) along with their ratio divided by 16 (gray), associated with the left axis, to show mass proportionality. The cartoon figure on the bottom right is adapted from M. D. McManus et al. (2022) for the case in this example; see details in the text.

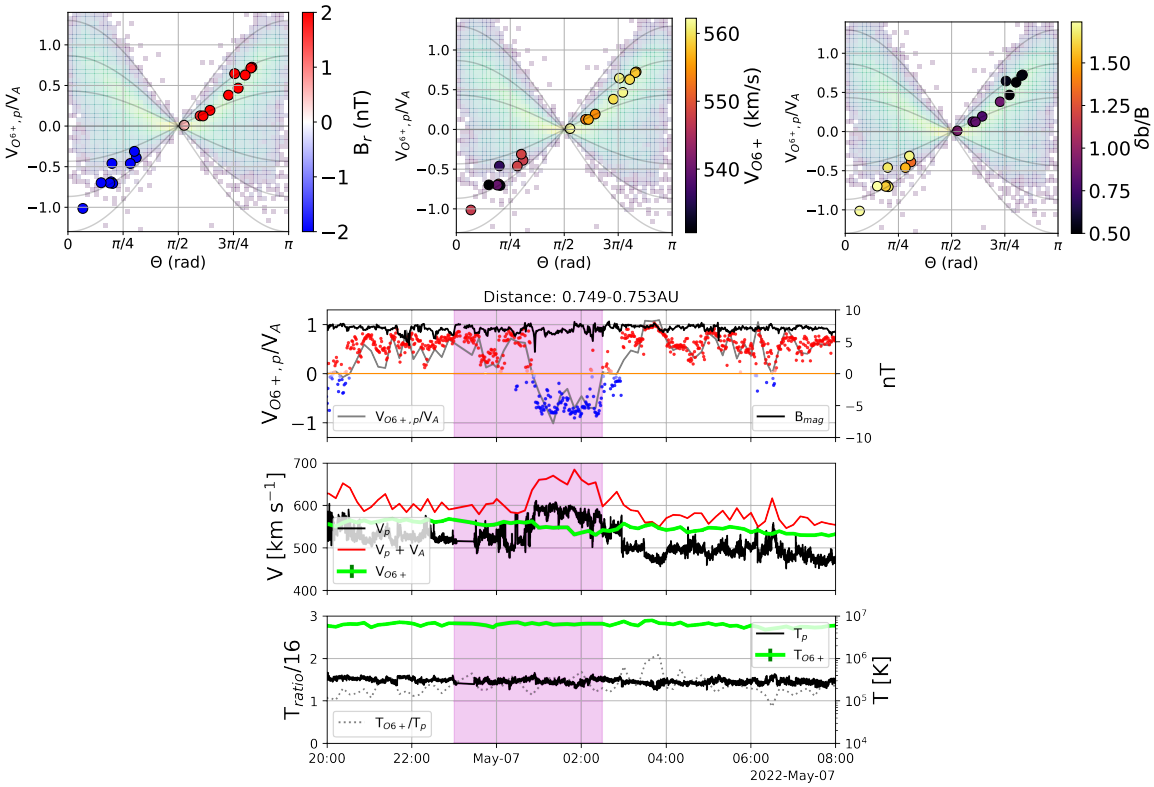

Figure 5. Same as Figure 4 but for a different case.

M. D. McManus et al. (2022) that predicts the velocity fluctuation behavior of He^{2+} for three scenarios where the alphas flow slower than (i), at the same speed as (ii), and faster than (iii) the local wave speed, which would result in an increase, no change, and a decrease in the alpha speed, respectively (see also L. Matteini et al. 2014, 2015; T. S. Horbury et al. 2018). We modify the image to include O^{6+} under the case of scenario (iii) in accordance with this example period. For the example fluctuation in Figure 4, we find that the O^{6+} behaves in accordance with the lever-arm scenario, where with an initial differential flow faster than the local Alfvén speed, the O^{6+} speed decreases, from 780 to 740 km s^{-1} (top middle panel), as would be predicted by the cartoon picture in the bottom right and our simple model calculation in Section 2.

However, for the second example shown in Figure 5, in solar wind farther from the Sun, we find that despite the O^{6+} differential flow speed being just below the Alfvén speed prior to the field rotation, the O^{6+} speed decreases during the fluctuation while it is predicted to increase. For the period, the initial $V_{O6+,p}/V_A$ is shown in each panel of the top row (starting in the top right portion of the plots) and observed to be lower than 1. For an O^{6+} differential flow speed of less than 1, the lever-arm behavior would indicate that the O^{6+} speed would increase under scenario (i) from M. D. McManus et al. (2022). However, as shown in the top middle panel, the O^{6+} speed decreases from 560 to 520 km s^{-1}. We interpret this as a case where the Alfvén speed calculated is larger than the actual wave speed, as has been previously discussed and observed in the solar wind (B. E. Goldstein et al. 1995; M. Neugebauer et al. 1996). Depending on the difference, a lower wave speed (V_w) versus V_A would increase the $V_{O6+,p}/V_w$ ratio computed prior to the fluctuation to a value larger than 1, indicating that scenario (iii) rather than (i) from M. D. McManus et al. (2022) would be compatible with observations. To explore this idea, we plot the magnetic field and velocity components, radial and perpendicular (projection of tangential and normal components as $B_\perp = \sqrt{B_T^2 + B_N^2}$ and $V_\perp = \sqrt{V_T^2 + V_N^2}$), illustrated in Appendix Figure C1. We find that the magnetic field components trace a circle (or a sphere in 3D) across the fluctuation as would be the case for spherically polarized Alfvén waves. The velocity fluctuation indicates that the motion of the components has more curvature in the perpendicular components compared to the magnetic field. However, the clumps of data trace at least two coherent spheres in 3D. An inner circle is a curve fitted to the velocity covering the inner part of the V_R and $V_\perp$ with a radius of 43.4 km s^{-1}, while $V_A = 62$ km s^{-1}. The substructure that traces different spherical shells across the fluctuation could potentially indicate a distinct wave and Alfvén speed and ultimately affect our lever-arm interpretation. Further analysis of individual cases across the different distances and wind speeds warrants its own detailed future study.

5. Conclusions and Outlook

We examine the radial evolution of the O^{6+} speed and temperature between 0.3 and 1 au within a 1.3 yr time frame of data collected by HIS on Solar Orbiter. The main conclusions of the study find that on average the following O6+ properties are observed:

1. Across all wind speeds, differential flow ($V_{O6+,p}$ and $V_{O6+,p}/V_A$) decreases with heliocentric distance from the Sun.
2. The temperature ratio (T_{O6+}/T_p) decreases with distance but remains super-mass-proportional (>16).
3. T_{O6+} cools adiabatically with increasing heliocentric distance across all wind speeds, suggesting that no significant heating is experienced by O^{6+} beyond 0.3 au.
4. Negative differential streaming, where O^{6+} tends to travel slower than the protons, increases with distance from the Sun and occurs during momentary kinks in the magnetic field that are commonly associated with large-amplitude Alfvénic fluctuations.
5. O^{6+} can differentially flow faster than the local Alfvén speed, and this is predominately observed to happen near perihelion periods, inside 0.57 au.

The temperature and speed radial profiles of O^{6+} (see Figure 2) are well organized across wind speed bins. However, no strong speed dependence is found except for O^{6+} temperature. The results indicate that O^{6+} behaves similarly to He^{2+} where the differential flow and its temperature ratio with protons decrease with heliocentric distance; however, unlike alphas, they show that no significant heating is experienced between 0.3 and 1 au, as indicated by the adiabatic scalar temperature profile.

As is evident in Figures 4 and 5, O^{6+} exhibits negative differential streaming during periods where large kinks in the magnetic field occur. Detailed examination of the oxygen speed across the magnetic fluctuation indicates its speed is reduced in cases where it is expected to increase, following the behavior of He^{2+} (B. E. Goldstein et al. 1995; L. Matteini et al. 2014, 2015; M. D. McManus et al. 2022; J. H. Wang et al. 2025). In future work, a detailed and higher-resolution examination of the speed of O^{6+} during Alfvénic fluctuations at different stages of the solar wind's radial evolution can provide valuable insight into wave–particle dynamics. In particular, careful determination of the local wave speed is key to understanding the behavior of O^{6+} during these fluctuations.

A comparison to remote observations of O^{5+} at the Sun (up to 3.5 and 5 $R_\odot$; see Figure 3) suggests that the superheated oxygen in the corona may peak in temperature and cool very shortly after the observed distances under the assumption of an adiabatic extrapolation back to the Sun, suggesting that the majority of heating happens below 0.3 au and the Alfvén surface. However, given that there is a huge gap between remote observations ending at 5 $R_\odot$ and 65 $R_\odot$ where O^{6+} is first observed in situ, it is unclear where a temperature peak occurs. For a complete picture across this region, there is a critical need for heavy ion observations below 0.3 au in both in situ as well as contemporaneous remote observations of heavy ion densities, temperatures, and outflow speeds from a next-generation UVCS-like instrument to bridge this gap (J. M. Laming & A. Vourlidas 2019; Y. J. Rivera et al. 2022; Y. J. Rivera & S. T. Badman 2025).

In summation, our observational findings show that the radial evolution of O^{6+}, the third most abundant ion species in the solar wind, differs from that of protons and He^{2+} in several key ways. It therefore places new constraints on multispecies models of solar wind heating and acceleration.

Acknowledgments

The authors thank Benjamin Chandran and Timothy Horbury for insightful discussion on the work. Y.J.R., S.T.B., and M.L.S. are partially supported by the Parker Solar Probe project through the SAO/SWEAP subcontract 975569. C.J.O. and D.V. were supported by STFC consolidated grant ST/W001004/1. K.G.K. is partially supported by NASA grant 80NSSC240171. B.L.A. acknowledges Solar Orbiter and Parker Solar Probe funding at NASA/GSFC and NASA/LWS funding under 80NSSC22K1011. J.T.C. was supported by STFC grant ST/W001071/1. J.H.W. is supported by the STFC under studentship ST/X508433/1.

Solar Orbiter is a mission of international cooperation between ESA and NASA, operated by ESA. Solar Orbiter SWA data were derived from scientific sensors that were designed and created and are operated under funding provided by numerous contracts from UKSA, STFC, the Italian Space Agency, CNES, the French National Centre for Scientific Research, the Czech contribution to the ESA PRODEX program, and NASA. SO SWA work at the UCL/Mullard Space Science Laboratory is currently funded by UKSA/STFC grants UKRI919 and UKRI1204. The SWA-HIS team acknowledges NASA contract NNG10EK25C.

Appendix A
Solar Orbiter Trajectory and Data Availability

Figure A1 shows the trajectory of Solar Orbiter within the HIS data availability period of 2022 January 1–2023 April 30. The period includes three perihelia, with closest approaches on 2022 March 26, 2022 October 12, and 2023 April 10. The light green periods highlighted along the trajectory show periods where HIS data were available.

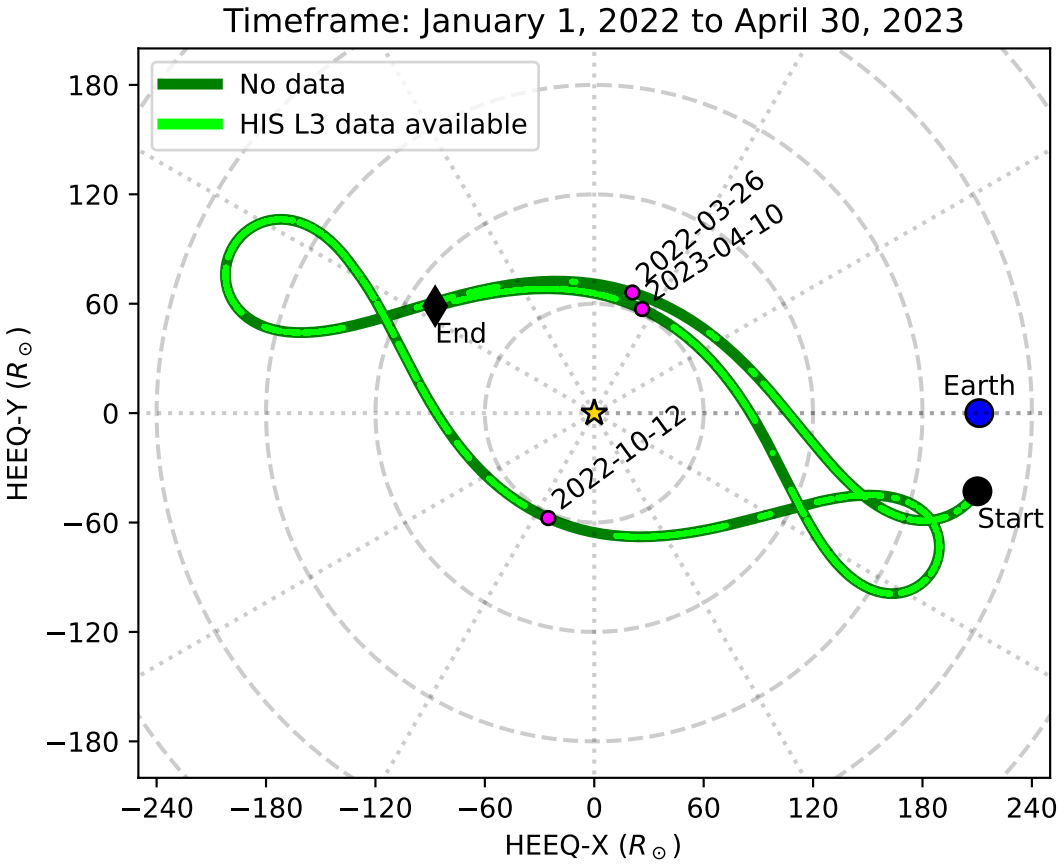

Figure A1. The orbital path of Solar Orbiter over the time frame covered in the analysis in this paper is plotted in dark green. The light green periods along the trajectory are locations where the HIS Level 3 data were available. The magenta markers and corresponding dates indicate perihelia.

Appendix B
Moth Plots Separated by Speed and Heliocentric Distance

Figures B1 and B2 show the same moth plots as Figure 1 except computed within various distance intervals from the Sun and in various solar wind speed ranges, as indicated above each panel. Further examining these properties separated by wind speed and distance from the Sun reveals the evolution of the solar wind within this parameter space. The period of interest is divided into four speed and three distance quantiles to ensure a statistically significant comparison between the panels. The ranges of speed and distance noted at the top of each plot are determined from the average data collected in each speed/location range, causing them to differ slightly. The different panels in the figure are arranged with an increasing distance from the Sun viewing left to right and increasing solar wind speed from top to bottom. The color bar for Figure B1 is counts, and for Figure B2, it is the average temperature ratio (T_{O6+}/T_p) in each bin. We note a few features in the distribution of points, on average.

1. Field-aligned differential streaming is maximum closest to the Sun across all solar wind speeds.
2. Solar wind with differential streaming larger than an Alfvén speed occurs at the closest distances to the Sun.
3. Differential streaming decreases with distance from the Sun within all solar wind speeds.
4. Negative differential streaming increases with growing distance from the Sun.

Pertaining to the temperature and differential streaming relationship, we find that the largest temperature ratio is observed closest to the Sun and in the slowest speed bin (top left of Figure 1 and also in Appendix Figure B2). However, all

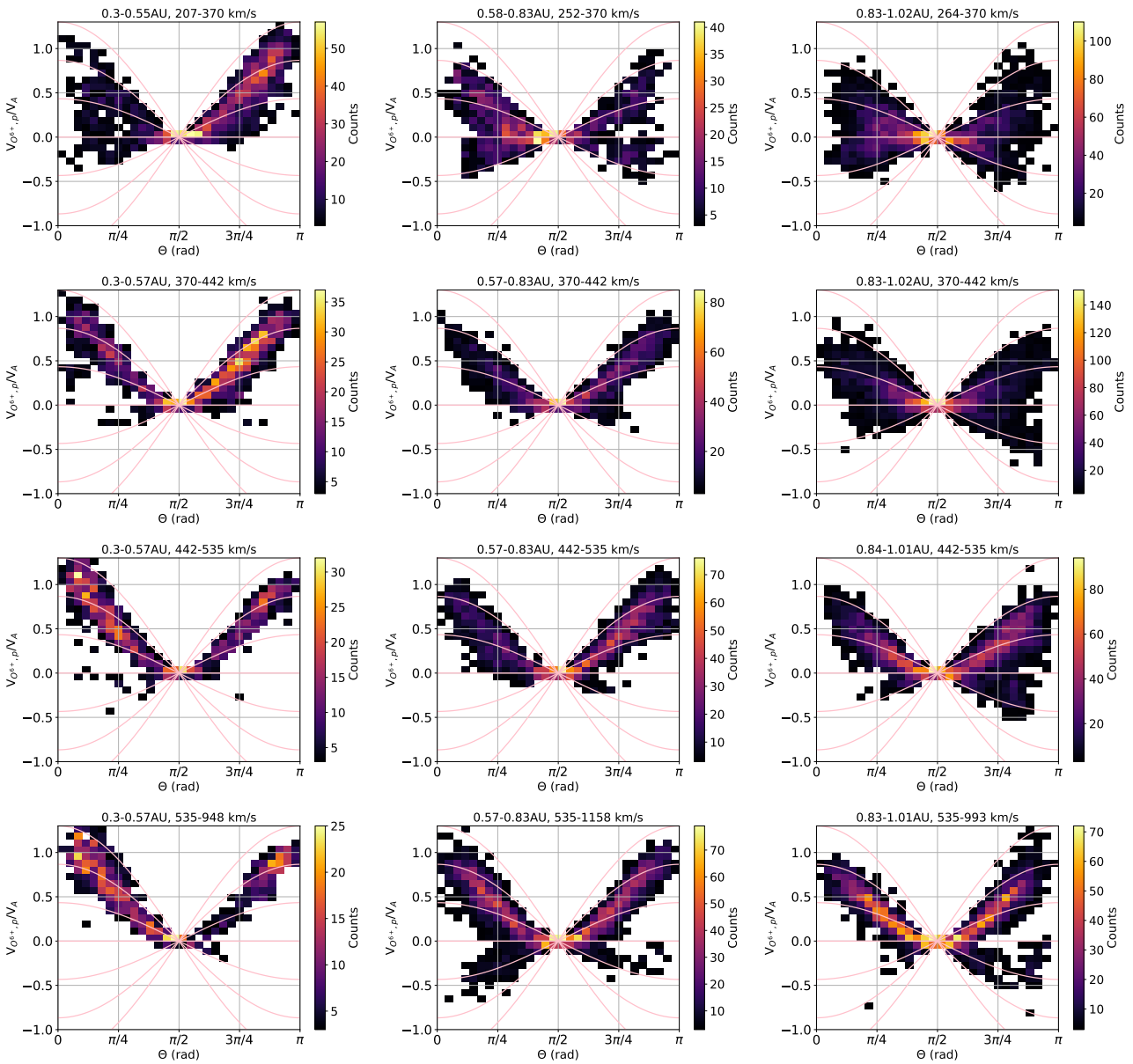

Figure B1. Moth plots of counts for differential streaming of O^{6+} normalized to the local Alfvén speed vs. angle between the flow direction and the local magnetic field, same as Figure B2.

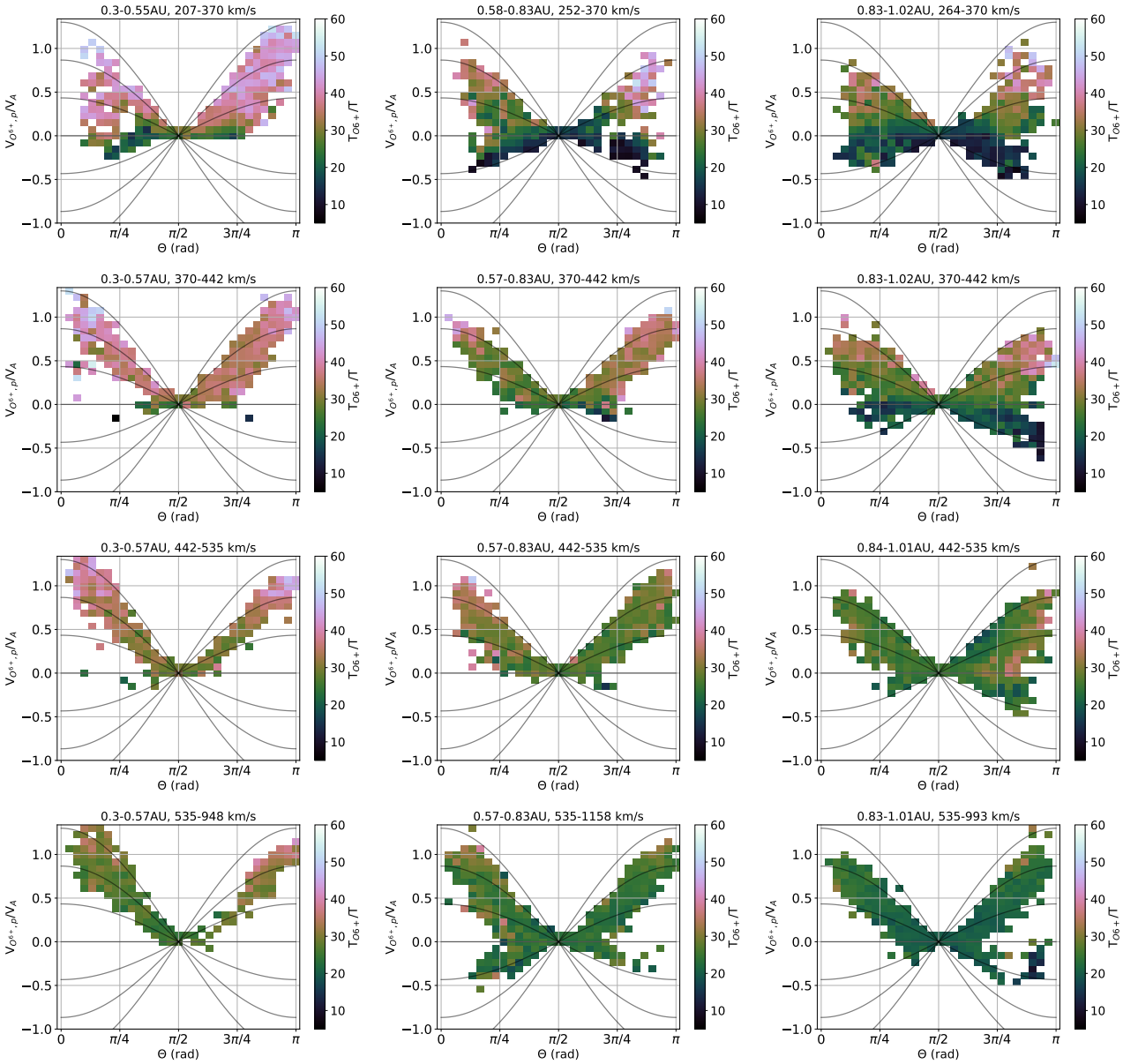

Figure B2. Moth plots, 2D histogram, of temperature ratio (T_{O6+}/T_p) for differential streaming of O^{6+} normalized to the local Alfvén speed vs. angle (Θ) between the radial direction and the local magnetic field direction. The color bar indicates the proton-to-O^{6+} temperature ratio (T_{O6+}/T_p), which is kept consistent across all panels and with Figure 1.

analyzed solar wind shows a decrease in the temperature ratio with larger heliocentric distances. We discuss this observation further in the following section. The fastest wind speeds (bottom row of Appendix Figure B2) show more uniformity in temperature ratio within changing differential streaming values overall, while the slowest wind contains a larger range of temperature, particularly at large Θ. The negative differential streaming region of the plot is generally lower in temperature ratio, as observed in the right panel of Figure 1.

Appendix C
Magnetic and Velocity Fluctuations across Alfvénic Fluctuation

Figure C1 shows the magnetic field (B_R and $B_\perp$) and velocity (V_R and $V_\perp$) components (left and right panels, respectively) across the shaded magenta region of Figure 5, as described in Section 4.4. The radius of the dashed circle (left panel) is the mean magnitude of the magnetic field, while the cyan circle in the right panel shows the mean Alfven speed, $V_A = 62\,\mathrm{km\,s^{-1}}$, and the two black circles are ± standard deviation of V_A. The red circle is a curve fitted to the velocity covering the inner part of the circle with a radius of $43.4\,\mathrm{km\,s^{-1}}$.

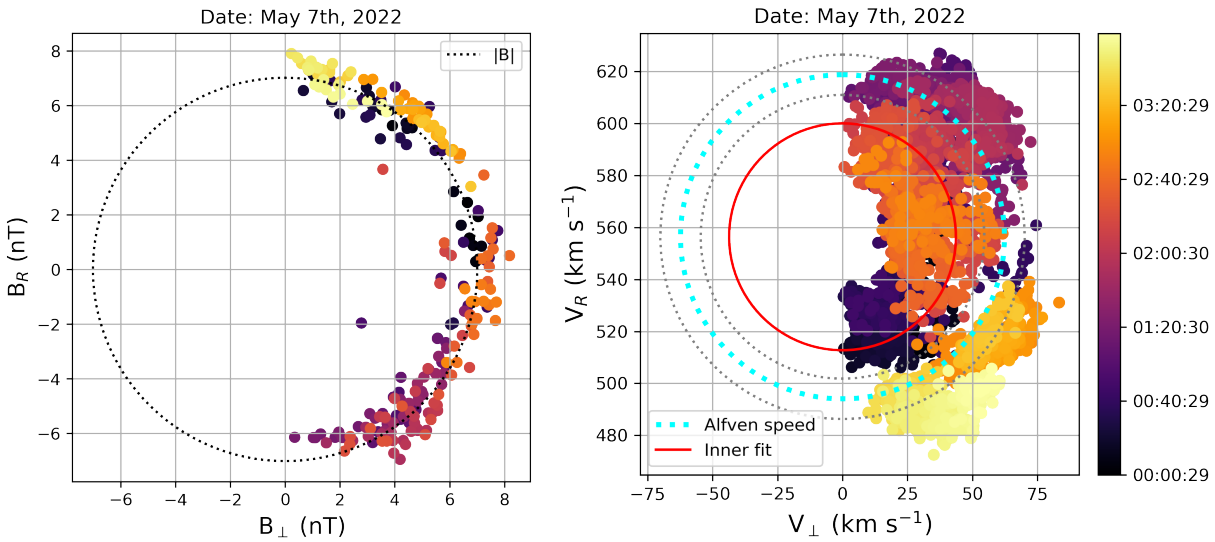

Figure C1. The magnetic field and velocity, radial (B_R, V_R), and perpendicular projections ($B_\perp$, $V_\perp$) during the shaded magenta region time frame of Figure 4, where the color of the points indicates the associated time.

Appendix D
Differential Streaming versus Alfvén Speed

Figure D1 (left panel) shows the distribution of $V_{O6+,p}$ versus Alfvén speed. As in the top row of Figure 2, we only include periods of differential streaming for $\Theta < 0.5$ and >2.5. The plot indicates a strong positive correlation between differential flow and V_A; however, it does not appear to saturate at the largest Alfvén speed as indicated by J. H. Wang et al. (2025) for He^{2+}. This is likely due to the proximity to the Sun, where the large majority of observations from J. H. Wang et al. (2025) are taken much closer than 0.3 au, while Solar Orbiter samples 0.3 and beyond. This is a strong indicator of the need for heavy ion observations below 0.3 au, where this phenomena occurs, for direct comparison to alpha particles.

Figure D1 (right panel) shows the radial profile of the Alfvén speed for the different speed bins from Figure 2. Similar to M. Neugebauer et al. (1996), the V_A profiles are shallower than a $1/r$ dependence across all wind speeds.

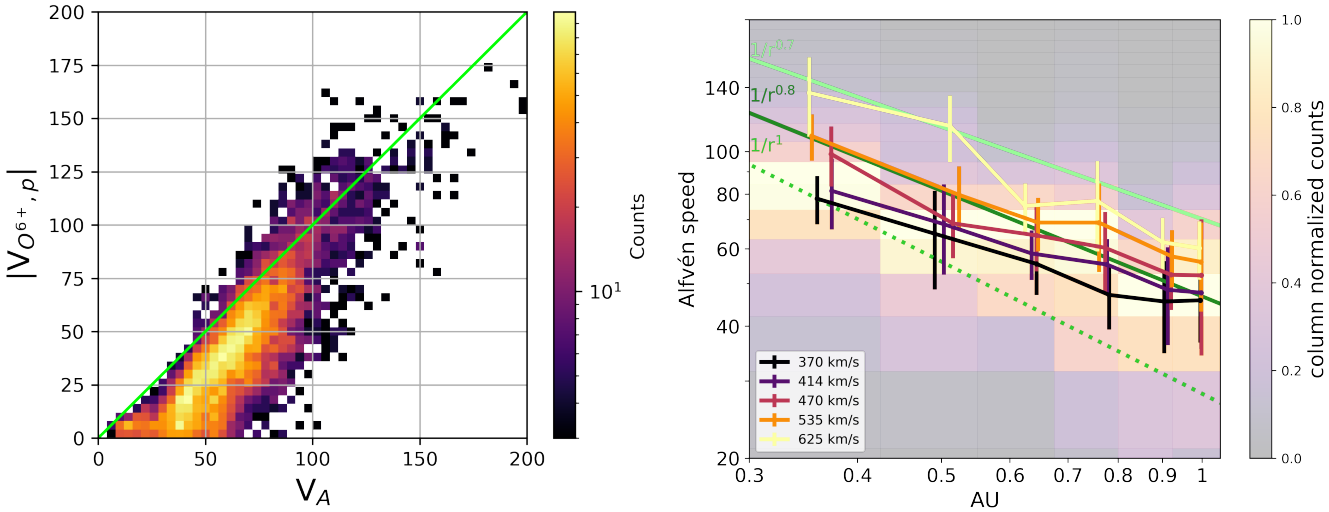

Figure D1. (Left) 2D histogram of counts of differential speed, $V_{O6+,p}$, against Alfvén speed, V_A. The green line has a slope of 1 showing correlation between the values. (Right) Radial evolution of Alfvén speed within the same speed bins as Figure 2. We include three power-law profiles, $1/r^{0.7}$, $1/r^{0.8}$, and $1/r^1$, for reference.

ORCID iDs

Yeimy J. Rivera https://orcid.org/0000-0002-8748-2123
Kristopher G. Klein https://orcid.org/0000-0001-6038-1923
Joseph H. Wang https://orcid.org/0009-0008-4095-9175
Lorenzo Matteini https://orcid.org/0000-0002-6276-7771
Daniel Verscharen https://orcid.org/0000-0002-0497-1096
Jesse T. Coburn https://orcid.org/0000-0002-2576-0992
Samuel T. Badman https://orcid.org/0000-0002-6145-436X
Susan T. Lepri https://orcid.org/0000-0003-1611-227X
Ryan M. Dewey https://orcid.org/0000-0003-4437-0698
Jim M. Raines https://orcid.org/0000-0001-5956-9523
B. L. Alterman https://orcid.org/0000-0001-6673-3432
Timothy J. Stubbs https://orcid.org/0000-0002-5524-645X
Kevin C. Delano https://orcid.org/0000-0002-9280-0480
Roberto Livi https://orcid.org/0000-0002-0396-0547
Stefano A. Livi https://orcid.org/0000-0002-4149-7311
Antoinette B. Galvin https://orcid.org/0000-0003-3752-5700
Christopher J. Owen https://orcid.org/0000-0002-5982-4667
Michael L. Stevens https://orcid.org/0000-0002-7728-0085

References

Abbo, L., Antonucci, E., Mikić, Z., et al. 2010, AdSpR, 46, 1400
Abbo, L., Ofman, L., Antiochos, S. K., et al. 2016, SSRv, 201, 55
Adhikari, L., Zank, G. P., Zhao, L. L., Nakanotani, M., & Tasnim, S. 2021, A&A, 650, A16
Alterman, B. L., Kasper, J. C., Stevens, M. L., & Koval, A. 2018, ApJ, 864, 112
Alterman, B. L., Rivera, Y. J., Lepri, S. T., & Raines, J. M. 2025a, A&A, 694, A265
Alterman, B. L., Rivera, Y. J., Lepri, S. T., Raines, J. M., & D'Amicis, R. 2025b, A&A, 700, A23
Ayaz, S., Li, G., & Khan, I. A. 2024, ApJ, 970, 140
Ayaz, S., Zank, G. P., Khan, I. A., Li, G., & Rivera, Y. J. 2025a, A&A, 694, A23
Ayaz, S., Zank, G. P., Khan, I. A., et al. 2025b, MNRAS, 540, 3583
Bandyopadhyay, R., Meyer, C. M., Matthaeus, W. H., et al. 2023, ApJL, 955, L28
Berger, L., Wimmer-Schweingruber, R. F., & Gloeckler, G. 2011, PhRvL, 106, 151103
Bochsler, P., Lee, M. A., Karrer, R., et al. 2010a, AnGeo, 28, 491
Bochsler, P., Lee, M. A., Karrer, R., et al. 2010b, AIP Conf. Ser. 1216, Twelfth Int. Solar Wind Conf., ed. M. Maksimovic et al. (Melville, NY: AIP), 257
Bourouaine, S., Perez, J. C., Chandran, B. D. G., et al. 2024, ApJL, 967, L19
Bowen, T. A., Bale, S. D., Chandran, B. D. G., et al. 2024b, NatAs, 8, 482
Bowen, T. A., Vasko, I. Y., Bale, S. D., et al. 2024a, ApJL, 972, L8
Carpenter, D. T., Lepri, S. T., Zhao, L., et al. 2024, FrASS, 11, 1472874
Chandran, B. D. G. 2010, ApJ, 720, 548
Chandran, B. D. G., Verscharen, D., Quataert, E., et al. 2013, ApJ, 776, 45
Cranmer, S. R. 2009, LRSP, 6, 3
Cranmer, S. R. 2020, RNAAS, 4, 249
Cranmer, S. R., Panasyuk, A. V., & Kohl, J. L. 2008, ApJ, 678, 1480
Cranmer, S. R., & van Ballegooijen, A. A. 2003, ApJ, 594, 573
Cranmer, S. R., & Winebarger, A. R. 2019, ARA&A, 57, 157
Durovcová, T., Sǎfrańková, J., & Němeček, Z. 2019, SoPh, 294, 97
Fox, N. J., Velli, M. C., Bale, S. D., et al. 2016, SSRv, 204, 7
Gary, S. P., Yin, L., Winske, D., & Reisenfeld, D. B. 2000, GeoRL, 27, 1355
Goldstein, B. E., Neugebauer, M., & Smith, E. J. 1995, GeoRL, 22, 3389
González, C. A., Tenerani, A., Matteini, L., Hellinger, P., & Velli, M. 2021, ApJL, 914, L36
Halekas, J. S., Bale, S. D., Berthomier, M., et al. 2023, ApJ, 952, 26
Hefti, S., Grünwaldt, H., Ipavich, F. M., et al. 1998, JGRA, 103, 29697
Hellinger, P., Velli, M., TráVníčEk, P., et al. 2005, JGRA, 110, A12109
Hollweg, J. V., & Isenberg, P. A. 2002, JGRA, 107, 1147
Holmes, J., Kasper, J., Klein, K. G., Lepri, S. T., & Raines, J. M. 2024, ApJ, 964, 19
Horbury, T. S., Matteini, L., & Stansby, D. 2018, MNRAS, 478, 1980
Horbury, T. S., O'Brien, H., Carrasco Blazquez, I., et al. 2020, A&A, 642, A9
Howes, G. G. 2024, JPlPh, 90, 905900504
Hu, Y. Q., & Habbal, S. R. 1999, JGRA, 104, 17045
Isenberg, P. A., & Vasquez, B. J. 2007, ApJ, 668, 546
Isenberg, P. A., & Vasquez, B. J. 2009, ApJ, 696, 591
Janitzek, N. P., Taut, A., Berger, L., et al. 2016, in AIP Conf. Ser. 1720, Solar Wind 14 Conf. Ser. 17 (Melville, NY: AIP), 040006
Kasper, J. C., & Klein, K. G. 2019, ApJL, 877, L35
Kasper, J. C., Klein, K. G., Weber, T., et al. 2017, ApJ, 849, 126
Kasper, J. C., Lazarus, A. J., & Gary, S. P. 2008, PhRvL, 101, 261103
Kasper, J. C., Maruca, B. A., Stevens, M. L., & Zaslavsky, A. 2013, PhRvL, 110, 091102
Kohl, J. L., Esser, R., Gardner, L. D., et al. 1995, SoPh, 162, 313
Laming, J. M., & Vourlidas, A. 2019, in AGU Fall Meeting Abstracts, 2019 (Washington, DC: American Geophysical Union), SH31B
Liu, W., Zhao, J., Wang, T., et al. 2023, ApJ, 951, 69
Livi, S., Lepri, S. T., Raines, J. M., et al. 2023, A&A, 676, A36
Marsch, E. 2006, LRSP, 3, 1
Marsch, E., Rosenbauer, H., Schwenn, R., Muehlhaeuser, K. H., & Neubauer, F. M. 1982a, JGRA, 87, 35
Marsch, E., Schwenn, R., Rosenbauer, H., et al. 1982b, JGRA, 87, 52
Marsch, E., & Tu, C. Y. 2001, JGRA, 106, 227
Martinović, M. M., Klein, K. G., De Marco, R., et al. 2025, ApJL, 988, L25
Martinović, M. M., Klein, K. G., Ďurovcová, T., & Alterman, B. L. 2021, ApJ, 923, 116
Maruca, B. A., Bale, S. D., Sorriso-Valvo, L., Kasper, J. C., & Stevens, M. L. 2013, PhRvL, 111, 241101
Maruca, B. A., Kasper, J. C., & Gary, S. P. 2012, ApJ, 748, 137
Matteini, L., Hellinger, P., Landi, S., Trávníček, P. M., & Velli, M. 2012, SSRv, 172, 373
Matteini, L., Horbury, T. S., Neugebauer, M., & Goldstein, B. E. 2014, GeoRL, 41, 259
Matteini, L., Horbury, T. S., Pantellini, F., Velli, M., & Schwartz, S. J. 2015, ApJ, 802, 11
Matteini, L., Landi, S., Hellinger, P., et al. 2007, GeoRL, 34, L20105
McManus, M. D., Klein, K. G., Bale, S. D., et al. 2024, ApJ, 961, 142
McManus, M. D., Verniero, J., Bale, S. D., et al. 2022, ApJ, 933, 43
Meyrand, R., Squire, J., Schekochihin, A. A., & Dorland, W. 2021, JPlPh, 87, 535870301
Mostafavi, P., Allen, R. C., McManus, M. D., et al. 2022, ApJL, 926, L38
Möstl, C., Isavnin, A., Boakes, P. D., et al. 2017, SpWea, 15, 955
Möstl, C., Weiss, A. J., Bailey, R. L., et al. 2020, ApJ, 903, 92
Müller, D., St. Cyr, O. C., Zouganelis, I., et al. 2020, A&A, 642, A1
Neugebauer, M., Goldstein, B. E., Smith, E. J., & Feldman, W. C. 1996, JGRA, 101, 17047
Owen, C. J., Bruno, R., Livi, S., et al. 2020, A&A, 642, A16
Panchal, U., Wicks, R. T., & Stawarz, J. E. 2025, ApJ, 983, 160
Peng, J., He, J., Duan, D., & Verscharen, D. 2024, ApJ, 977, 27
Raymond, J. C., Kohl, J. L., Noci, G., et al. 1997, SoPh, 175, 645
Reisenfeld, D. B., Gary, S. P., Gosling, J. T., et al. 2001, JGRA, 106, 5693
Rivera, Y. J., & Badman, S. T. 2025, arXiv:2502.06036
Rivera, Y. J., Badman, S. T., Stevens, M. L., et al. 2024, Sci, 385, 962
Rivera, Y. J., Badman, S. T., Verniero, J. L., et al. 2025, ApJ, 980, 70
Rivera, Y. J., Higginson, A., Lepri, S. T., et al. 2022, FrASS, 9, 417
Schwartz, S. J., & Marsch, E. 1983, JGR, 88, 9919
Shankarappa, N., Klein, K. G., Martinović, M. M., & Bowen, T. A. 2024, ApJ, 973, 20
Silwal, A., Zhao, L., Zhu, X., et al. 2025, ApJS, 278, 40
Sioulas, N., Shi, C., Huang, Z., & Velli, M. 2022, ApJL, 935, L29
Squire, J., Meyrand, R., Kunz, M. W., et al. 2022, NatAs, 6, 715
Tracy, P. J., Kasper, J. C., Raines, J. M., et al. 2016, PhRvL, 116, 255101
Tracy, P. J., Kasper, J. C., Zurbuchen, T. H., et al. 2015, ApJ, 812, 170
Tu, C. Y., & Marsch, E. 1995, SSRv, 73, 1
Verniero, J. L., Larson, D. E., Livi, R., et al. 2020, ApJS, 248, 5
Verscharen, D., Bourouaine, S., & Chandran, B. D. G. 2013, ApJ, 773, 163
Verscharen, D., Klein, K. G., & Maruca, B. A. 2019, LRSP, 16, 5
Wang, J. H., Horbury, T. S., Matteini, L., & Trotta, D. 2025, ApJL, 978, L17
Zhang, M. F., Kunz, M. W., Squire, J., & Klein, K. G. 2025, ApJ, 979, 121